In Situ Monitoring of Catalytic Molecular Transformations on Noble Metal Nanocatalysts Using Surface-Enhanced Raman Spectroscopy

Hui Wang*, Qingfeng Zhang, Esteban Villarreal, Hao Jing, and Kexun Chen

Department of Chemistry and Biochemistry, University of South Carolina, 631 Sumter Street, Columbia, South Carolina 29208, United States

Noble metal nanoparticles have long been of tremendous interest in the nanophotonics and nanocatalysis communities owing to their intriguing size- and shape-dependent plasmonic and catalytic properties. The combination of tunable plasmon resonances with superior catalytic activities on the same noble metal nanoparticle, however, has long been challenging because the research on nanoplasmonics and nanocatalysis deals with nanoparticles in two drastically different size regimes. While tunable plasmon resonances are a unique feature of metallic nanoparticles in the sub-wavelength size regime, heterogeneous catalysis requires the use of substrate-supported sub-5 nm nanoparticulate catalysts. In this mini-review article, we share with the readers several approaches we recently developed toward the realization of plasmonic-catalytic dual-functionalities on a single noble metal nanoparticle. Our approaches involve judicious tailoring of the atomic-level surface structures of sub-wavelength plasmonic nanoparticles through either kinetically controlled seed-mediated nanocrystal growth or regioselective surface etching. These structurally tailored, dual-functional nanoparticles serve as both substrates for surface-enhanced Raman spectroscopy (SERS) and free-standing nanoparticulate catalysts. Using SERS as a molecular finger-printing spectroscopic tool, we have been able to track detailed structural evolution of molecular adsorbates in real time during catalytic reactions. The quantitative insights gained from the *in situ* SERS measurements shed light on the detailed relationships between interfacial molecule-transforming behaviors and the atomic-level surface structures of noble metal nanocatalysts.

Introduction

While noble metals, such as Au, Ag, Pt, and Pd, are all precious materials, they may become even more "precious" when their dimensions are reduced to the nanoscale owing to the emergence of unique optical and catalytic properties that are otherwise unobservable in their bulk counterparts. Noble metal nanoparticles (NMNPs) exhibit highly tunable optical properties that are dominated by the resonantly excited free electron oscillations, known as plasmons. By tailoring the size, shape, composition, and local environment of NMNPs, the plasmon resonance frequencies can be fine-tuned over a broad spectral range spanning the visible and near-infrared regions, offering unique opportunities for applications in photonics, sensing, and biomedicine.[1-5] An optically excited plasmonic nanoparticle may also function as a nanoscale antenna that concentrates light into ultrasmall volumes in close proximity to the particle surfaces, creating electromagnetic "hot spots" with enormous local-field enhancements exploitable for plasmon-enhanced spectroscopies.[6-9] Besides their fascinating optical characteristics, NMNPs, especially multimetallic alloys and heteronanostructures, have also aroused rapidly growing interest in the heterogeneous catalysis community because they represent a family of catalyst materials whose structural and compositional parameters can be systematically tuned to achieve the optimal catalytic performance toward specific reactions.[10-12]

Development of detailed mechanistic understanding of NMNP-based catalysis relies critically on our capability to precisely monitor the molecular transformations occurring on catalyst surfaces in real time. Surface-enhanced Raman scattering (SERS) provides an ultrasensitive, non-invasive plasmon-enhanced vibrational spectroscopic tool ideal for detailed structural characterizations of molecular adsorbates residing in the plasmonic hot spots on NMNP surfaces.[7-9] SERS-based *in situ* monitoring of catalytic reactions requires dual functionalities that merge desired plasmonic and catalytic properties on the same NMNPs, which has long been a challenging task because plasmonics and catalysis require the use of NMNPs in two drastically different size regimes. Tunable plasmon resonances are a unique feature of NMNPs in the sub-wavelength size regime typically ranging from tens of nanometers to submicrons, whereas heterogeneous catalysis requires the use of much smaller nanoparticulate catalysts in the sub-5 nm size regime. The most straightforward strategy to realize plasmonic-catalytic dual-functionalities on the same nanoscale entity is to assemble catalytically active sub-5 nm NMNPs on or near the surfaces of sub-wavelength plasmonic nanostructures to form suprananostructures.[13-17] Although these dual-functional suprananostructures enable SERS-based reaction monitoring, it still remains challenging to elucidate the detailed structure-property relationships underpinning the materials performance and the interfacial molecular behaviors because of the intrinsic structural complexity of the suprananostructures and additional complication arising from multimodal interactions between the discrete functional units.

This mini-review article epitomizes the mechanistic insights on NMNP-catalysis we recently gained through deliberately designed *in situ* SERS measurements. The key to the success of our research endeavor is the integration of desired plasmonic and catalytic properties on dual-functional single-component nanoparticles, which serve as both SERS substrates and free-standing catalysts. Our synthetic approaches to the dual-functional NMNPs involve fine-engineering of the surface atomic coordination and configurations of plasmonically tunable sub-wavelength nanoparticles through either seed-mediated nanocrystal growth or regioselective surface etching under kinetically controlled conditions. Monitoring NMNPs-catalyzed reactions *in situ* using SERS as a unique molecular finger-printing tool allows us to correlate detailed interfacial molecule-transforming behaviors to the atomic-level surface structures of the nanocatalysts.

Surface Textured Au Nanoparticles

The intriguing size-dependent catalytic behaviors of NMNPs have been best manifested by Au nanocatalysts. Although Au is catalytically inert in the form of bulk materials, ultrasmall Au nanoparticles with diameters below ~ 5 nm exhibit remarkable catalytic activities toward a diverse set of reactions.[18-20] When serving as the catalysts, these sub-5 nm Au nanoparticles are typically dispersed on high-surface-area oxide supports to suppress the particle sintering under operando conditions. Interestingly, the oxide materials supporting the Au nanocatalysts may further enhance the overall catalytic activities through various mechanisms involving particle-support and molecule-support interactions.[21-24] While several aspects regarding detailed mechanisms dictating the size-dependent catalytic behaviors of Au still remain ambiguous, it has become increasingly evident that the undercoordinated surface atoms, which are highly abundant on the locally curved surfaces of sub-5 nm Au nanoparticles, serve as the primary active sites for catalysis.[20, 25-26] When Au nanoparticles become larger than 5 nm, their catalytic activity rapidly decays and diminishes owing to the low fraction of undercoordinated atoms exposed on their surfaces. Despite their limited catalytic activity, these larger Au nanoparticles show strong, tunable plasmon resonances with intense local field enhancements exploitable for SERS. In contrast, sub-5 nm metallic nanoparticles exhibit weak plasmon resonances featured by broadened extinction spectral lineshapes and diminished scattering and absorption features.[27]

We bridged this intrinsic gap between the two particle size regimes required for catalysis and plasmonics by creating nanoscale textures on the surfaces of sub-wavelength Au nanoparticles.[28] Sub-wavelength quasi-spherical nanoparticles (QSNPs) represent a thermodynamically

favored geometry whose surfaces are dominated by energetically stable, low-index facets, such as {111} and {100} facets, with only a small fraction of undercoordinated surface atoms located at the surface defect sites and the crystalline domain boundaries (Figure 1A). Through deliberate kinetic control of the seed-mediated nanocrystal growth, we were able to synthesize Au surface-roughened nanoparticles (SRNPs), a kinetically favored meta-stable structure. Au SRNPs are rich of undercoordinated surface atoms at the locally curved surface sites (Figure 1B-1E), well-mimicking the local surface structures of the catalytically active, sub-5 nm nanoparticles. Au SRNPs also exhibited greatly enhanced size-dependent plasmonic tunability (Figure 1F) and remarkably higher local field enhancements in comparison to Au QSNPs (Figure 1G and 1H). When the nanoparticle plasmons were tuned to be on resonance with the excitation laser, apparent Raman enhancements on the order of 10^6 were achieved on individual Au SRNPs, more than 3 orders of magnitude higher than those on individual Au QSNPs.[29] Therefore, Au SRNPs represent a unique dual-functional materials system ideal for SERS-based spectroscopic monitoring of catalytic reactions.

We compared the catalytic activities of colloidal Au SRNPs and QSNPs toward the hydrogenation of 4-nitrophenol (4-NP) by borohydride in aqueous environment, a prototypical model reaction widely used for assessing the catalytic performances of metallic nanocatalysts. The reaction progress can be tracked in real time straightforwardly using UV-vis absorption spectroscopy because the reactant, 4-NP, and the final product, 4-aminophenol (4-AP), display distinct characteristic absorption peaks at 400 nm and 320 nm, respectively. Our UV-vis absorption spectroscopic results clearly showed that colloidal Au SRNPs exhibited surface-specific catalytic activities commensurate with those of ultrasmall Au nanoparticles (~ 2 nm in diameter) even though their overall particle sizes are in the catalytically inactive size regime (> 100 nm). However, the UV-vis absorption spectroscopic results neither precisely reflected the intrinsic catalytic activity of the Au nanocatalysts nor provided detailed molecular-level information regarding the multi-step reaction mechanisms. To gain deeper insights, we used a confocal Raman spectrometer/microscope setup to track the molecule transformations during catalytic hydrogenation of self-assembled monolayers (SAMs) of 4-nitrothiophenol (4-NTP) pre-immobilized on the surfaces of colloidal nanoparticles through time-resolved SERS measurements.

Our SERS-based approach has several unique advantages. (1) The plasmonic properties of the colloidal nanoparticles can be fine-optimized to generate intense local field enhancements that allow us to fine-resolve the spectral features of monolayer and sub-monolayer molecular adsorbates at the molecule-catalyst interfaces, enabling identification of transient reaction intermediates that are difficult to resolve through other means. (2) The reactant molecules were pre-immobilized on the nanocatalyst surfaces through covalent metal-thiol interactions, which makes it possible to unravel the intrinsic surface reaction kinetics with minimal complication caused by the molecular diffusion, adsorption, desorption, and ligand exchange occurring at the catalyst-solution interfaces. (3) Performing SERS measurements on colloidal samples allows us to quantitatively evaluate the intrinsic catalytic activities of free-standing metallic nanocatalysts without any complication caused by the support materials. (4) Using a confocal Raman microscope allows us to collect SERS signals from colloidal nanoparticle suspensions within an excitation volume as small as ~100 fL. The limited exposure time of each diffusing nanoparticle to the confocal laser beam effectively minimized sample damage caused by photothermal heating and suppressed plasmon-driven photoreactions.

Figures 2A shows the temporal evolution of SERS spectra during the catalytic reaction. 4-NTP chemisorbed on the surfaces of Au SRNPs exhibited three characteristic SERS peaks at 1080, 1338, and 1571 cm^{-1}, corresponding to C-S stretching (ν_{CS}), O-N-O stretching (ν_{NO}), and the aromatic ring stretching modes, respectively. At the initiate stage, we observed an induction time during which all the 4-NTP SERS features remained unchanged. The induction time was tied to the molecular oxygen dissolved in solution, which prohibited the adsorption of borohydride ions to the Au surfaces.[30] After the dissolved oxygen was consumed, borohydride started to interact with the Au surfaces to form

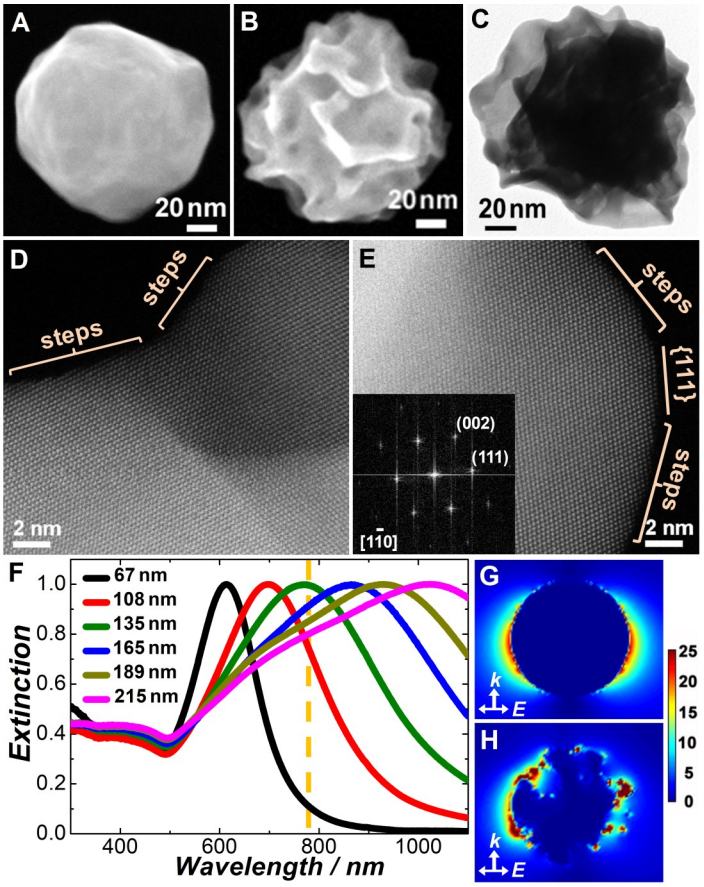

Figure 1. Scanning electron microscopy (SEM) images of an Au (A) QSNP and (B) SRNP. (C) Transmission electron microscopy (TEM) image of an Au SRNP. (D, E) High angle annular dark-field scanning transmission electron microscopy (HAADF-STEM) images highlighting the atomic-level surface structures of an Au SRNP. The inset in panel E is the fast Fourier transform pattern of the HAADF-STEM image. Reprinted with permission from ref [28]. Copyright 2014, American Chemical Society. (F) Optical extinction spectra of colloidal Au SRNPs with various average particle diameters as labeled in the figure. The vertical dash line indicates the wavelength of excitation laser for SERS measurements. Cross-sectional view of the local field enhancements of an Au (G) QSNP and (H) SRNP with a diameter of 135 nm at 785 nm plane wave excitation calculated using the Finite-Difference Time Domain (FDTD) method. Reprinted with permission from ref [29]. Copyright 2014, American Chemical Society.

Au hydride species. After the surface coverage of metal hydride was built up to a certain threshold value, the catalytic hydrogenation of the surface-adsorbed 4-NTP was initiated. As the reaction proceeded, the peak intensities of both the 1338 and 1571 cm^{-1} modes progressively decreased, while a new band corresponding to the phenol-ring modes (ν_{CC}) of 4-ATP at 1590 cm^{-1} emerged and became more intense. The characteristic vibrational modes of 4,4′-dimercaptoazobenzene (DMAB) at 1140, 1388, and 1438 cm^{-1} were clearly resolved at the intermediate stage of the reactions, indicating that DMAB was the intermediate along the reaction pathway. While the SAMs of 4-NTP and DMAB were stable on the surfaces of Au SRNPs, the final product, 4-ATP, dissociated from the particle surfaces in the presence of excessive $NaBH_4$, as the characteristic peaks of the ν_{CS} (1080 cm^{-1}) and ν_{CC} (1590 cm^{-1}) modes of 4-ATP both gradually decreased in intensity upon the completion of the hydrogenation reaction. Based on the temporal evolutions of several characteristic SERS peaks (Figure 2B), we proposed a four-step reaction mechanism (Figure 2C): (1) generation of Au hydride species through interactions between borohydride ions and metal surfaces, which gave rise to the induction time; (2) reduction of

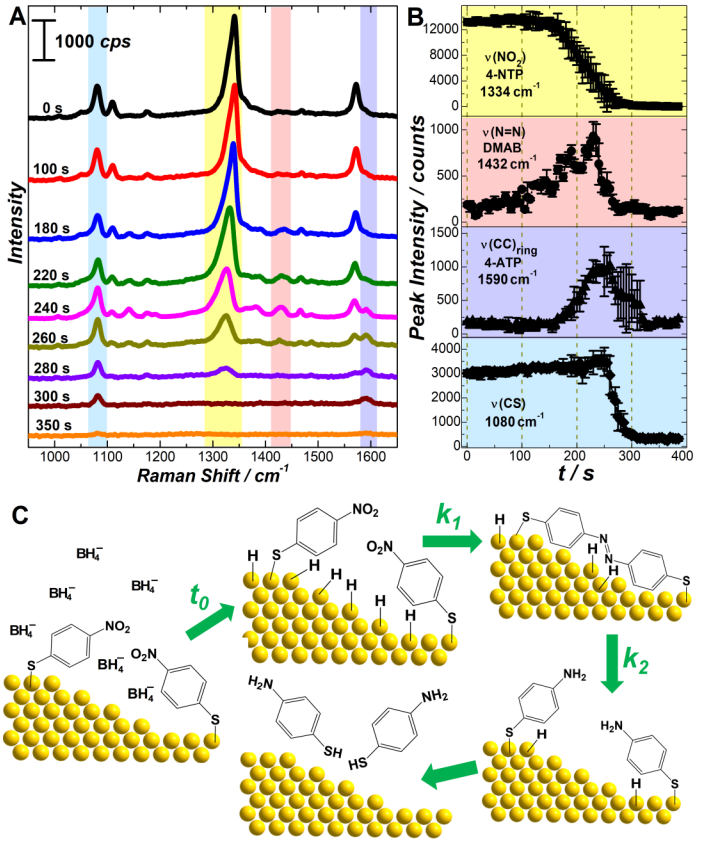

Figure 2. (A) SERS spectra collected from 4-NTP-coated Au SRNPs at different reaction times of 0, 100, 180, 220, 240, 260, 280, 300, and 350 s after exposure to 30 mM $NaBH_4$ in an aqueous solution at room temperature. (B) Temporal evolutions of the intensities of various SERS peaks at 1334, 1432, 1590, and 1080 cm^{-1}. (C) Schematic illustration of the mechanism of the catalytic hydrogenation reaction. Reprinted with permission from ref [28]. Copyright 2014, American Chemical Society.

surface-adsorbed 4-NTP by the surface hydride to form DMAB; (3) further reduction of DMAB into 4-ATP; and (4) desorption of 4-ATP from the nanocatalyst surfaces.

The desorption of 4-ATP from the surfaces of Au SRNPs can be interpreted in the context of nanoscale surface curvature effects.[31] The energetics and dynamics of the ligand-surface interactions are drastically modified when nanoscale curvatures are introduced to the planar Au surfaces. Through *in situ* SERS measurements, we found that the binding behaviors of thiolated ligands to atomically flat Au surfaces could be well-described using the classic Langmuir adsorption model, exhibiting much stronger binding affinity than to nanocurved surfaces. Although thermodynamically less favored, the binding of thiolated ligand molecules to the locally curved Au surfaces was kinetically faster, exhibiting a non-classic adsorption behavior with high binding cooperativity. These results imply that the local curvature on nanoparticle surfaces is a key structural parameter we can adjust to further fine-optimize the nanoparticle-molecule interfaces for catalysis.

High-Index Faceting Au Nanocrystals

The SERS results collected on colloidal Au SRNPs clearly showed that the undercoordinated surface atoms served as the primary active sites for catalyzing the hydrogenation of 4-NTP. However, it still remained challenging to quantitatively correlate the catalytic activity to the surface atomic configurations because the surface structures of Au SRNPs were highly sophisticated with a spatially heterogeneous distribution of surface atoms adopting a diverse set of atomic coordination numbers. This motived us to conduct a detailed comparative study on the catalytic activities of polyhedral Au nanocrystals enclosed by specific crystallographic facets with characteristic surface atomic configurations.

We are particularly interested in high-index faceting Au nanoparticles whose surfaces are rich of coordinatively unsaturated atoms at the surface steps and kinks. Although thermodynamically less stable, high-index facets exhibit remarkably higher catalytic activities toward a variety of reactions than those of the low-index facets terminated with close-packed surface atoms.[32] We chose single-crystalline Au elongated tetrahexahedral (ETHH), concave cubic (CC), and trisoctahedral (TOH) nanoparticles as three representative model nanostructures, each of which was exclusively enclosed by one specific type of high-index facets.[33] The ETHH geometry can be derived from a cuboid by creating surface convexity on each {100} facet (Figure 3A). Through kinetically controlled seed-mediated nanocrystal growth, we synthesized colloidal ETHH nanoparticles each of which was enclosed by 24 high-index {730} facets (Figure 3B). A CC nanoparticle was geometrically derived by introducing tetragonal indentation to each {100} facet of a nanocube (Figure 3C). Each of the Au CC nanoparticles synthesized through seed-mediated growth was enclosed by 24 high-index {520} facets (Figure 3D). A TOH nanoparticle was derived from a nano-octahedron by creating a trigonal pyramid on each triangular {111} facet (Figure 3E). The Miller index of the exposed facets on the surfaces of experimentally synthesized Au TOH nanoparticles was identified to be {221} (Figure 3F). The Au ETHH, CC, and TOH nanocrystals were all in the sub-wavelength size regime with well-defined facets significantly larger than 5 nm in size, ensuring that the catalytic activities were essentially tied to the characteristic distribution of undercoordinated surface atoms on each type of facets rather than those at the particle corners and edges. Sub-wavelength Au ETHH, CC, and TOH NPs all exhibited appealing plasmonic properties, exhibiting size-dependent plasmon resonances and significantly higher SERS enhancements than the low-index faceting QSNPs primarily due to the presence of vertices on their surfaces.[34] Therefore, these high-index faceting nanocrystals provided an ideal materials system for us to quantitatively compare the intrinsic catalytic activities of three types of high-index facets, {730}, {520}, and {221} facets, through *in situ* SERS measurements.

Figure 3G shows the geometric models illustrating the atomic-level surface structures of high-index {730}, {520}, {221} facets, on the basis of which the fractions of surface atoms with specific coordination numbers can be calculated. No surface desorption of final product, 4-ATP, was observed upon completion of the reactions, indicating that 4-ATP molecules were bound more strongly to the high-index facets than to the nanotextured surfaces of SRNPs. Therefore, we were able to track the fraction trajectories of both 4-NTP and 4-ATP in real time according to the temporal evolution of SERS peak intensities at 1338 and 1590 cm^{-1}. Under our experimental conditions, this catalytic reaction obeyed pseudo-first-order kinetics following the rate laws for a two-step consecutive reaction.

$$\theta_R = e^{-k_1 \times (t-t_0)} \quad (1),$$

$$\theta_P = 1 + \frac{k_1 \times e^{-k_2 \times (t-t_0)} - k_2 \times e^{-k_1 \times (t-t_0)}}{k_2 - k_1} \quad (2),$$

$$\theta_I = 1 - \theta_R - \theta_P \quad (3),$$

where θ_R and θ_P were the fraction of reactant (4-NTP) and product (4-ATP), respectively. θ_I was the fraction of the intermediate (DMAB). t was the reaction time. t_0 was the induction time. k_1 and k_2 were the rate constants for the first and second hydrogenation steps, respectively. In Figure 3H, we directly compared the k_1 and k_2 values for various Au facets. Because k_2 was significantly larger than k_1, θ_I remained low during the reactions. However, the high detection sensitivity of SERS and the intrinsically large Raman cross-section of DMAB allowed us to clearly identify DMAB as the intermediate and fully resolve the kinetics of the two-step reaction. All the high-index facets were catalytically

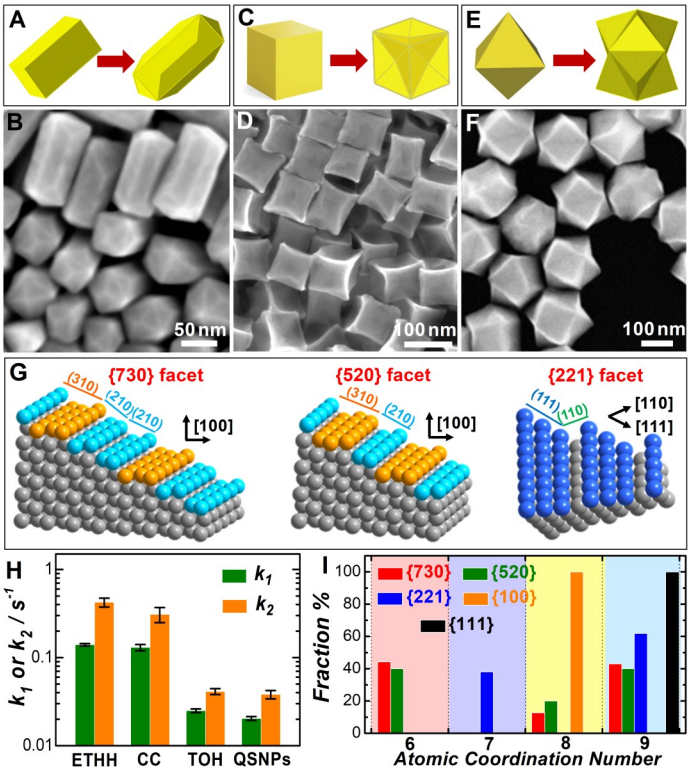

Figure 3. (A) Geometric models of a nanocuboid and an ETHH nanoparticle. (B) SEM image of ETHH nanoparticles. (C) Geometric models of a nanocube and a CC nanoparticle. (D) SEM image of CC nanoparticles. (E) Geometric models of an octahedral nanoparticle and a TOH nanoparticle. (F) SEM image of TOH nanoparticles. (G) Schemes of the atomic level surface structures of the high-index {730}, {520}, and {221} facets. (H) Comparison of the rate constants, k_1 and k_2, of the two-step hydrogenation reactions on Au ETHH, CC, TOH nanocrystals and QSNPs. (I) Fraction of the surface atoms with various coordination numbers on the {730} (ETHH), {520} (CC), {221} (TOH), and {111}/{100} (QSNPs) facets. Reprinted with permission from ref [33]. Copyright 2014, American Chemical Society.

more active than the low-index {111} and {100} facets. The catalytic activity of Au surfaces increased with decrease in surface atomic coordination numbers (Figure 3I), displaying a general trend of {730} > {520} > {221} > {100}/{111}. Our results provided clear experimental evidence verifying the crucial roles of undercoordinated Au surface atoms in catalyzing the nitro-aromatic compound hydrogenation reactions.

Regioselective Surface Etching of Ag Nanostructures

Substituting Au and the Pt-group metals with Ag significantly reduces the cost of catalyst materials because Ag is more earth-abundant and less expensive than the other noble metals. Although chemically less stable, Ag nanoparticles offer multiple advantages for plasmonic applications as they have far stronger plasmon resonances, wider plasmonic tuning range, and more intense local field enhancements than those achievable on the other noble metal counterparts. This motivated us to study the facet-dependent catalytic activity of Ag nanocatalysts using SERS as a plasmon-enhanced spectroscopic tool. However, controlled synthesis of high-index faceting Ag nanocrystals has been significantly more challenging because undercoordinated surface atoms of Ag are thermodynamically less stable than their Au and Pt counterparts and are thus, more difficult to retain during nanocrystal growth. Our strategy of integrating desired plasmonic and catalytic properties on the same Ag nanostructure is to create high-index facets on sub-wavelength Ag nanoparticles through regioselective surface etching.[35]

Our synthetic approach to the high-index faceting Ag nanostructures is schematically illustrated in Figure 4A. We chose Au@Ag core-shell nanocuboids enclosed by thermodynamically stable low-index {100} facets as the starting materials. By regioselectively etching the nanocuboid surfaces, we were able to create catalytically active high-index facets on the particle surfaces while maintaining the capability to fine-tune the plasmonic properties of the nanoparticles. Au@Ag core-shell nanocuboids were synthesized through epitaxial growth of Ag on the surfaces of single-crystalline Au nanorods. The nanocuboids underwent oxidative etching preferentially at the particle corners and edges upon exposure to Cu^{2+}, ascorbic acid (AA), and cetyltrimethylammonium chloride (CTAC) in an aqueous environment at 65 °C, gradually evolving into rice-shaped nanoparticles. CTAC served as a structure-directing surface-capping agent that selectively passivated the Ag {100} facets against etching. When the nanocuboids were exposed to Fe^{3+} and cetyltrimethylammonium bromide (CTAB), fast etching of the Ag {100} facets occurred, while the etching of the edges and corners were observed to be significantly slower than the side facet indentation, leading to the formation of dumbbell-shaped nanoparticles.

The geometric evolution of nanoparticles during etching caused systematic spectral shifts of the plasmon resonances. When the nanoparticle plasmons were tuned to be on resonance with the excitation laser at 785 nm, large local field enhancements were achieved on the

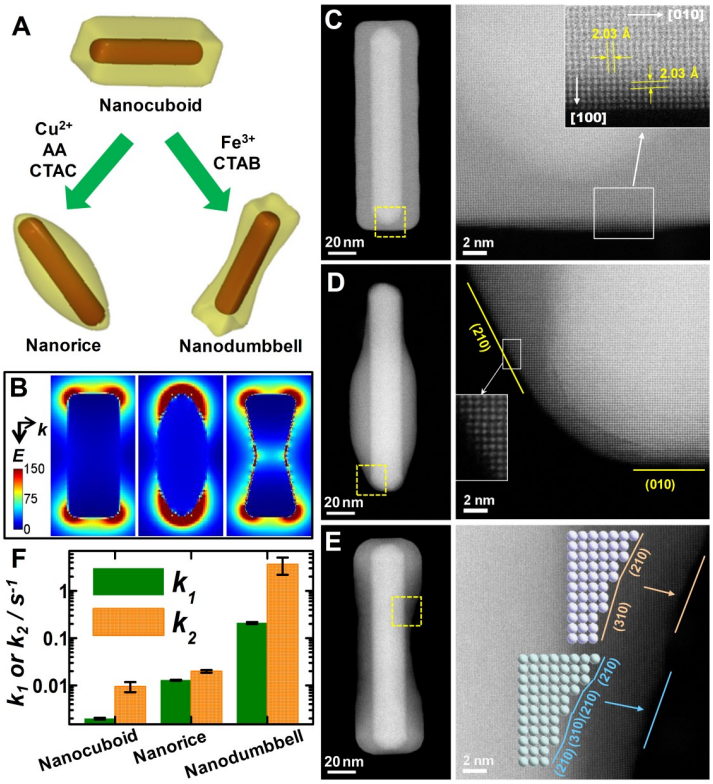

Figure 4. (A) Schematic illustration of regioselective etching of Au@Ag core-shell nanocuboids. (B) FDTD-calculated cross-sectional views of the local field enhancements of a nanocuboid (left), nanorice (middle), and nanodumbbell (right) upon excitation of their longitudinal plasmons at 785 nm. HAADF-STEM images of a (C) nanocuboid, (D) nanorice, and (E) nanodumbbell. The left panels show the images of individual particles and the right panels show the high-resolution images of the regions enclosed by the yellow squares in the left panels. (F) Comparison of k_1 and k_2 of the two-step hydrogenation reactions catalyzed by nanocuboid, nanorice and nanodumbbell particles. Reprinted with permission from ref [35]. Copyright 2014, American Chemical Society.

surfaces of nanocuboids, nanorice, and nanodumbbells (Figure 4B), giving rise to strong SERS enhancements. The regioselective nanoscale etching of nanocuboids also resulted in the formation of high-index facets at the etched surface sites. Prior to etching, a nanocuboid was enclosed by 6 {100} facets with some slight truncations at its edges and corners (Figure 4C). After a nanocuboid was etched into a nanorice particle, various well-defined high-index facets, such as {210} and {310} facets, formed on the particle surfaces (Figure 4D). Multiple stepped and kinked surfaces composed of localized high-index facets with Miller indices of {310}, {410}, {510}, and {610} were found at the tips and sides of the nanodumbbell particle (Figure 4E). The mechanism of the catalytic hydrogenation of 4-NTP on Ag surfaces appeared similar to that on Au surfaces, with DMAB and 4-ATP serving as the intermediate and final product, respectively. Both nanorice and nanodumbbells exhibited drastically enhanced catalytic activities in comparison to the nanocuboids due to the presence of high-index facets on the particle surfaces. Nanodumbbells exhibited the highest catalytic activity with k_1 approximately 10 times higher than that of nanorice particles and 2 orders of magnitude higher than that of the low-index faceting nanocuboids.

Kinetically controlled seed-mediated nanocrystal growth and regioselective surface etching provided two distinct pathways to create high densities of undercoordinated atoms on NMNP surfaces. Interestingly, oxidative etching and nanocrystal growth may interplay with each other to synergistically guide the versatile structural evolution of NMNPs under kinetically controlled conditions. Recently, we found that the nanoscale surface topography of shape-controlled Au nanocrystals could be fine-tailored through deliberate kinetic control of oxidative etching with respect to nanocrystal growth (Figure 5).[36] Our experimental observations strongly indicated that oxidative etching must be added as a pivotal missing piece to the puzzle to fully decipher the complex mechanisms underpinning the intriguing structural evolution of nanocrystals under the foreign ion- and surfactant-coguided seed-mediated growth conditions. Nanoscale surface texturing of sub-wavelength metallic nanoparticles greatly expands the plasmonic tuning range and enhances the local electric fields exploitable for SERS. Meanwhile, the surface-textured nanocrystals are enclosed by highly abundant undercoordinated surface atoms, which may serve as the active sites for heterogeneous catalysis. Therefore, judicious coupling of nanocrystal growth with regioselective oxidative etching enables structural control of NMNPs at a higher level of sophistication, greatly enhancing our capabilities to further fine-optimize the optical and catalytic properties of nanoparticles for specific applications.

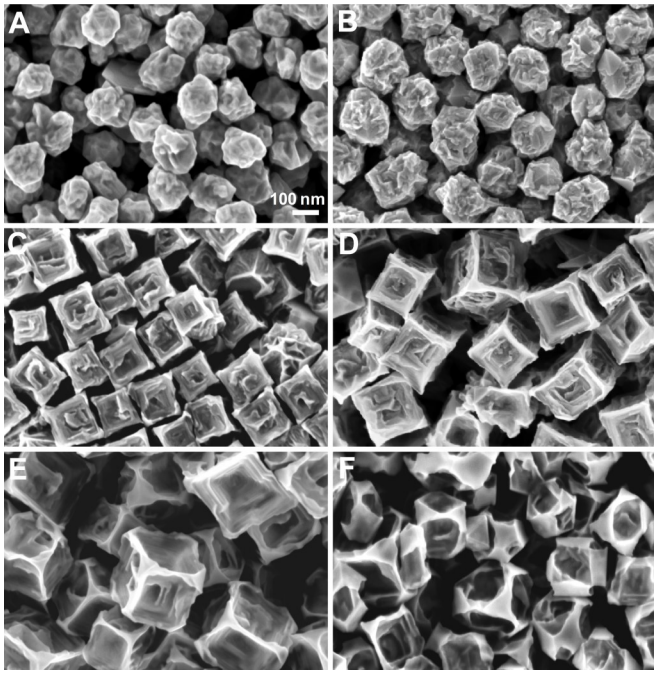

Figure 5. SEM images of Au nanoparticles synthesized after 16 h in growth solutions containing 100 mM CTAC, 50 μM $AgNO_3$, 500 μM $HAuCl_4$, and 1.2 mM AA at various HCl concentrations: (A) 0, (B) 2, (C) 5, (D) 10, (E) 15, and (F) 20 mM. As the HCl concentration increases, the relative rates of oxidative etching *vs.* nanocrystal growth increases. All SEM images share the same scale bar in panel A. Reprinted with permission from ref [36]. Copyright 2018, Royal Society of Chemistry.

Facet Control Of Au Nanorods

Au nanorods are anisotropic nanostructures with tunable plasmonic properties and built-in catalytic activities. The state-of-the-art colloidal synthesis of single-crystalline Au nanorods exhibiting a cylindrical morphology involves seed-mediated anisotropic nanocrystal growth co-guided by a foreign metal ion, Ag^+, and halide-containing cationic surfactants, typically CTAB.[37] This seed-mediated synthetic approach offers excellent control over the aspect ratios of Au nanorods, enabling fine-tuning of the longitudinal plasmon resonance (free electron oscillations along the longitudinal axis of the nanorods) in the visible and near-infrared spectral regions. Upon optical excitation of the longitudinal plasmons, the local electric fields can be enormously enhanced at the rod tips, providing hot-spots for SERS. Although generally described as a cylindrical nano-object with two rounded ends, experimentally synthesized Au nanorods essentially exhibit multifaceted surfaces enclosed by a mixture of various types of high-index and low-index facets. Heterogeneous site-specific catalytic activities were recently observed on individual single-crystalline Au nanorods, which were intimately tied to the geometric distribution of various local facets and defects on the nanorod surfaces.[38] Quantitative assignment of the crystallographic facets on the nanorod surfaces, however, has long been a widely debated subject.[39-41] While the locally curved nanorod surfaces are rich of catalytically active sites, it remains challenging to quantitatively correlate the catalytic activities to the atomic-level surface structures due to the intrinsic structural complexity and poor control over the nanorod facets.

We have been particularly interested in creating well-defined crystallographic facets with specific Miller indices on the surfaces of single-crystalline Au nanorods. We found that shape-controlled overgrowth of cylindrical Au nanorods guided by Cu^{2+} and cationic surfactants led to the formation of various anisotropic Au nanostructures each of which was enclosed exclusively by one specific type of low-index or high-index facets.[42] Our success in facet control of Au nanorods essentially relied on selective modification of the surface energies of various Au facets by Cu^{2+} ions and surface capping surfactants. Our key findings are schematically illustrated in Figure 6A. Cylindrical Au nanorods evolved into Au nanocuboids (NCBs) upon overgrowth in the presence of Cu^{2+} and CTAC. Overgrowth of Au nanorods in the benzyldimethylhexadecylammonium chloride (BDAC)/CTAC binary surfactant system resulted in Au convex nanocuboids (CVNCBs), whereas Au concave nanocuboids (CCNCBs) were obtained in the presence of CTAB/CTAC binary surfactants. While each NCB was enclosed by 6 low-index {100} facets, both CVNCBs and CCNCBs were high-index faceting nanostructures, each of which was enclosed by 24 {*hk0*}-type ({730} for CVNCB and {830} for CCNCB) high-index facets (Figure 6B-6D). Creation of well-defined facets on plasmonically tunable Au nanorods provided unique opportunities of using SERS to fine-resolve the molecule-transforming processes during catalytic hydrogenation of 4-NTP by ammonia borane (Figure 6E and 6F). Both CVNCBs and CCNCBs exhibited significantly higher activities than NCBs. On all three nanostructures, the conversion of 4-NTP into DMAB was observed to be the rate-limiting step. The undercoordinated surface atoms on high-index facets facilitated the surface-adsorption of ammonia borane, and thus served as catalytically more active sites for the hydrogenation reaction than the close-packed surface atoms on the low-index facets. The ratios between the two rate constants, k_1 and k_2, which determined the fraction of DMAB, could be effectively modulated by either tuning the facets of Au nanocatalysts or by changing the concentration of ammonia borane.

Using the {*hk0*}-faceting CVNCBs, also terms as elongated tetrahexahedral (ETHH) nanoparticles, as the starting materials, we further demonstrated that an entire family of high-index and low-index

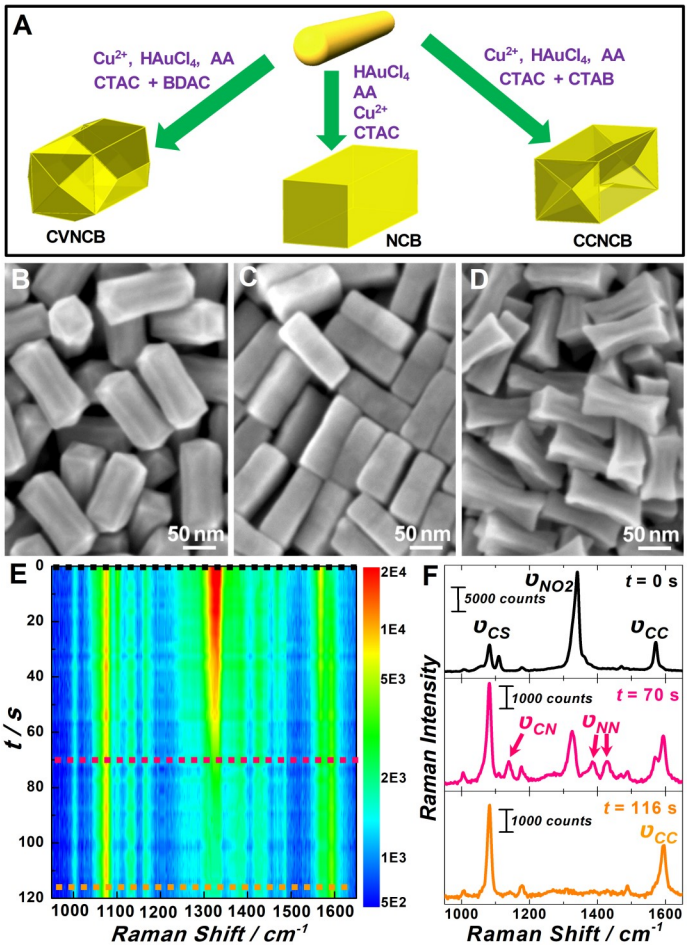

Figure 6. (A) Scheme illustrating the formation of Au NCBs, CVNCBs, and CCNCBs through overgrowth of cylindrical Au nanorods. SEM images of Au (B) CVNCBs, (C) NCBs, and (D) CCNCBs. (E) Temporal evolution of SERS spectra after exposing 4-NTP-coated CVNCBs to 2 mM ammonia borane at room temperature. (F) SERS spectra at reaction times of 0, 70, and 116 s. Reprinted with permission from ref [42]. Copyright 2015, American Chemical Society.

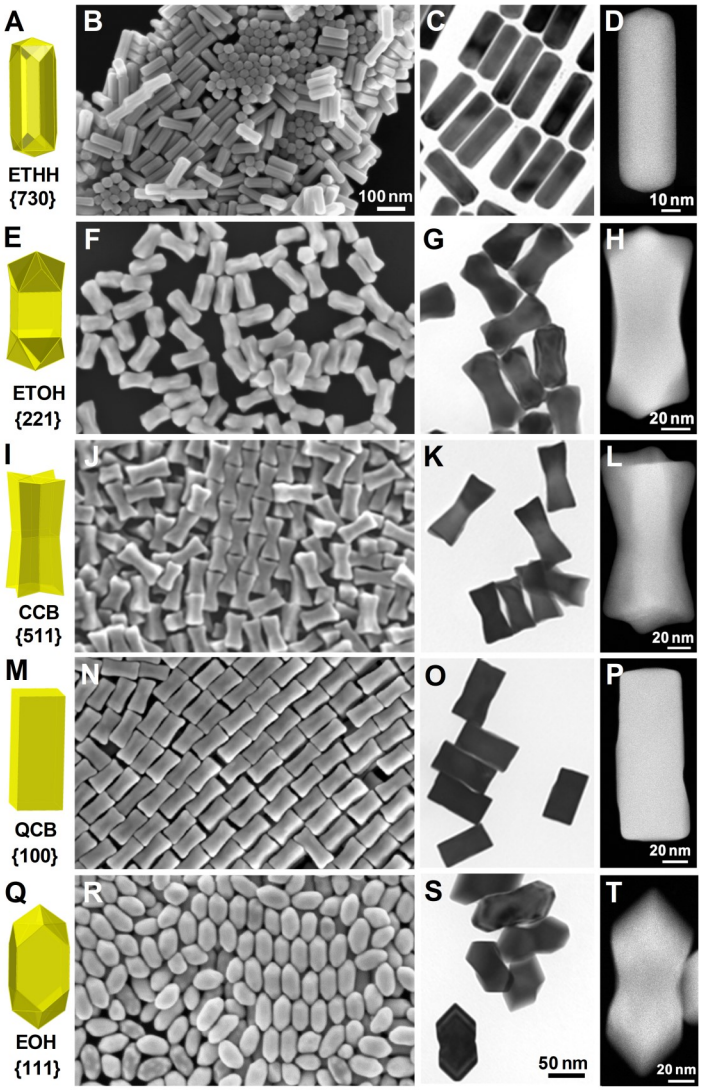

Figure 7. (A) Geometric model, (B) SEM, (C) TEM, and (D) HAADF-STEM images of Au ETHH nanoparticles. (E) Geometric model, (F) SEM, (G) TEM, and (H) HAADF-STEM images of Au ETOH nanoparticles. (I) Geometric model, (J) SEM, (K) TEM, and (L) HAADF-STEM images of Au CCB nanoparticles. (M) Geometric model, (N) SEM, (O) TEM, and (P) HAADF-STEM images of Au QCB nanoparticles. (Q) Geometric model, (R) SEM, (S) TEM, and (T) HAADF-STEM images of Au EOH nanoparticles. All the SEM images share the same scale bar in panel B. All the TEM images share the same scale bar in panel S. Reprinted with permission from ref [43]. Copyright 2016, American Chemical Society.

facets can be controllably created on the surfaces of single-crystalline nanorods using cuprous ions and CTAB as a unique pair of surface capping competitors to judiciously maneuver the thermodynamic and kinetic factors dictating the nanorod overgrowth.[43] We found that a series of interesting nanorod-derived geometries enclosed by well-defined characteristic high-index and low-index facets, such as {*hhk*}-faceting elongated trisoctahedral (ETOH) NPs, {*hkk*}-faceting concave cuboidal (CCB) NPs, as well as low-index faceting quasi-cuboidal (QCB) and elongated octahedral (EOH) nanoparticles, could be synthesized in a highly selective and controllable manner by systematically varying the molar ratio between Cu^{2+} and CTAB in the overgrowth solution (Figure 7). The Miller indices of the characteristic facets at the ends of the ETHH, ETOH, CCB, QCB, and EOH nanoparticles were {730}, {221}, {511}, {100}, and {111}, respectively. By exciting the longitudinal plasmon resonances, we were able to use SERS to monitor the catalytic reactions occurring on the end facets because the local field enhancements were confined at the two ends of these anisotropic nanostructures. The three types of high-index facets were catalytically much more active than the low-index facets toward the catalytic hydrogenation of 4-NTP. The {730} facets on ETHH nanoparticles exhibited the highest catalytic activities among all the nanostructures we investigated, with k_1 approximately 500 times larger than that of the EOH nanoparticles enclosed by the least active {111} facets. Both k_1 and k_2 were observed to be facet dependent, decreasing in the order of {730} > {511} > {221} > {100} > {111}. k_1 was much more sensitively dependent upon the facets than k_2. The observed facet-dependent catalytic activities correlated well with the characteristic distributions of undercoordinated surface atoms on various facets, with lower surface-atomic coordination number giving rise to higher catalytic activity toward the hydrogenation reaction. These faceted Au nanorods, which exhibited fine-tailored atomic-level surface structures while still inheriting the plasmonic tunability of the conventional cylindrical Au nanorods, served as a unique multifunctional nanomaterials system that allowed us to quantitatively correlate the intrinsic catalytic activities with the atomic-level surface structures of Au nanocatalysts using SERS as a time-resolving spectroscopic tool.

Summary and Outlook

As exemplified by the case studies described above, the integration of desired plasmonic and catalytic properties on the same NMNPs can be experimentally realized through deliberately designed colloidal syntheses that enable precise control of the atomic-level surface structures and fine-tuning of the plasmonic properties of the nanoparticles. These dual-functional nanoparticles serve as both the substrates for SERS and the catalysts boosting the reactions, allowing us to use SERS as an *in situ* spectroscopic tool to fine-resolve the molecular structural evolution during catalytic reactions and develop quantitative understanding of detailed reaction mechanisms. The knowledge gained from *in situ* SERS measurements, coupled with the detailed surface structural information obtained from electron microscopy imaging, form the foundation that allows us to precisely correlate the intrinsic catalytic behaviors to the surface atomic configurations of metallic nanocatalysts. Using the hydrogenation of 4-NTP catalyzed by structure-controlled monometallic Au and Ag nanoparticle surfaces as a model reaction, we have clearly shown the crucial roles of undercoordinated surface atoms in noble metal-based heterogeneous catalysis. The work summarized in this mini-review article provides a proof-of-concept clearly demonstrating the feasibility of using SERS for *in situ* monitoring of catalytic reactions on NMNPs. Built upon the insights extracted from our previous work, we are currently exploring the structure-property relationships of more complex materials systems, such as alloy nanocatalysts and multimetallic heteronanostructures. The SERS-based approach can also be used as a generic *in situ* spectroscopic tool for detailed mechanistic investigations of a large variety of catalytic, electrocatalytic, and photocatalytic molecule-transforming processes that are directly relevant to fuel production, energy conversion, and environmental remediation. At the end of this mini-review article, we briefly mention some of our latest progress in these relevant areas to highlight the value of SERS as an *in situ* spectroscopic tool for investigating catalysis, electrocatalysis, and photocatalysis.

Multimetallic nanoparticles exhibit remarkably further enhanced structural, optical, and catalytic tunabilities in comparison to their monometallic counterparts. Precise structural control of multimeallic nanocrystals represent a synthetically more challenging task because the nucleation and growth of multimetallic nanoparticles involve substantially more complicated structure-transforming processes due to the interplay of multiple thermodynamic, kinetic, and geometric factors. We recently demonstrated that single-crystalline cylindrical Au nanorods selectively transformed into a series of structurally distinct Au-Pd and Au-Ag bimetallic anisotropic nanostructures with interesting geometric, compositional, and plasmonic characteristics through kinetically controlled, seed-mediated coreduction processes.[44-45] These bimetallic nanostructures exhibit exotic multifaceted geometries enclosed by specific types of facets with fine-tailored surface compositional stoichiometries. The success in precise facet and composition control and the capability of using SERS to track catalytic reactions in real time will further allow us to investigate the detailed correlation between the surface structures (atomic coordinations, alloys *vs.* intermetallics, interfacial lattice strain in heteronanostructures), the compositional stoichiometries, and the catalytic behaviors of colloidal multimetallic nanocatalysts.

Beside chemical catalysis, NMNPs also exhibit excellent electrocatalytic performance toward a variety of electrochemical reactions directly relevant to clean fuel production and fuel cell operation. Over the past few years, we have been focusing on the structure-property relationship underpinning the electrocatalytic behaviors of dealloyed nanoporous metallic nanostructures.[46-49] These sponge-like metallic nanostructures also exhibit interesting plasmonic properties highly desired for SERS[50] and local photothermal heating.[51] We envision that SERS will serve as a power tool to resolve detailed molecular transformations occurring at the electrode/electrolyte interfaces.

NMNPs have also been of tremendous interest in the photocatalysis community. On one hand, the plasmon resonances of NMNPs may greatly enhance the photocatalytic activity of nearby semiconductor photocatalysts through various mechanisms.[52-53] One the other hand, the non-thermally distributed hot carriers generated during nonradiative plasmon decay can be effectively harnessed to drive intriguing photocatalytic transformations of molecules directly adsorbed on the NMNP surfaces along unconventional pathways fundamentally distinct from those involved in conventional thermal catalysis and exciton-driven photocatalysis.[54] Recently, we used SERS as a unique *in situ* spectroscopic tool to precisely monitor exciton- and plasmonic hot electron-driven photocatalytic reactions occurring on the surfaces of rationally designed plasmonic suprananostructures.[55-56] Plasmon-driven and plasmon-enhanced photocatalysis is an emerging area full of challenges and open questions. Using SERS to monitor the interfacial photocatalytic molecular transformations in real time allows us to pinpoint - with unprecedented precision and detail - the effects of plasmon excitations, molecular adsorption states, local field enhancements, and photothermal processes on the reaction pathways and kinetics. The mechanistic insights gained from *in situ* SERS measurements will provide new design principles for the next generation noble-metal based photocatalysts.

Acknowledgements

This work was supported by the National Science Foundation through awards DMR-1253231 and OIA-1655740 and the University of South Carolina through Startup Funds, an ASPIRE-I Track 1 Award, and an ASPIRE-I Track 4 Award. Q.Z. was partially supported by a Dissertation Fellowship provided by the NanoCenter of the University of South Carolina. E.V. was partially supported by a Department of Education Graduate Assistance in Areas of National Need (GAANN) Fellowship through Award P200A120075.

Notes and References

**Corresponding author email: wang344@mailbox.sc.edu (H. Wang)*
Phone: 1-803-777-2203; Fax: 1-803-777-9521

1. Wang, H.; Brandl, D. W.; Nordlander, P.; Halas, N. J. Plasmonic Nanostructures: Artificial Molecules. Acc. Chem. Res. 2007, 40 (1), 53-62.
2. Jain, P. K.; Huang, X. H.; El-Sayed, I. H.; El-Sayed, M. A. Noble Metals on the Nanoscale: Optical and Photothermal Properties and Some Applications in Imaging, Sensing, Biology, and Medicine. Acc. Chem. Res. 2008, 41 (12), 1578-1586.
3. Halas, N. J.; Lal, S.; Chang, W. S.; Link, S.; Nordlander, P. Plasmons in Strongly Coupled Metallic Nanostructures. Chem. Rev. 2011, 111 (6), 3913 -3961.
4. Jing, H.; Zhang, L.; Wang, H. Geometrically Tunable Optical Properties of Metal Nanoparticles. In UV-Vis and Photoluminescence Spectroscopy for Nanomaterials Characterization, Kumar, C., Ed. Springer Berlin Heidelberg: Berlin, Heidelberg, 2013; pp 1-74.
5. Anker, J. N.; Hall, W. P.; Lyandres, O.; Shah, N. C.; Zhao, J.; Van Duyne, R. P. Biosensing with Plasmonic Nanosensors. Nat. Mater. 2008, 7 (6), 442-453.
6. Willets, K. A.; Van Duyne, R. P. Localized Surface Plasmon Resonance Spectroscopy and Sensing. Annu. Rev. Phys. Chem. 2007, 58, 267-297.
7. Nie, S. M.; Emery, S. R. Probing Single Molecules and Single Nanoparticles by Surface-Enhanced Raman Scattering. Science 1997, 275 (5303), 1102-1106.
8. Fang, Y.; Seong, N. H.; Dlott, D. D. Measurement of the Distribution of Site Enhancements in Surface-Enhanced Raman Scattering. Science 2008, 321 (5887), 388-392.
9. Li, J. F.; Huang, Y. F.; Ding, Y.; Yang, Z. L.; Li, S. B.; Zhou, X. S.; Fan, F. R.; Zhang, W.; Zhou, Z. Y.; Wu, D. Y.; Ren, B.; Wang, Z. L.; Tian, Z. Q. Shell-Isolated Nanoparticle-Enhanced Raman Spectroscopy. Nature 2010, 464 (7287), 392-395.
10. Chen, M. S.; Goodman, D. W. The Structure of Catalytically Active Gold on Titania. Science 2004, 306 (5694), 252-255.
11. Chen, C.; Kang, Y. J.; Huo, Z. Y.; Zhu, Z. W.; Huang, W. Y.; Xin, H. L. L.; Snyder, J. D.; Li, D. G.; Herron, J. A.; Mavrikakis, M.; Chi, M. F.; More, K. L.; Li, Y. D.; Markovic, N. M.; Somorjai, G. A.; Yang, P. D.; Stamenkovic, V. R. Highly Crystalline Multimetallic Nanoframes with Three-Dimensional Electrocatalytic Surfaces. Science 2014, 343 (6177), 1339-1343.
12. Zhang, L.; Roling, L. T.; Wang, X.; Vara, M.; Chi, M. F.; Liu, J. Y.; Choi, S. I.; Park, J.; Herron, J. A.; Xie, Z. X.; Mavrikakis, M.; Xia, Y. N. Platinum-Based Nanocages with Subnanometer-Thick Walls and Well-Defined, Controllable Facets. Science 2015, 349 (6246), 412-416.
13. Xie, W.; Herrmann, C.; Kompe, K.; Haase, M.; Schlucker, S. Synthesis of

Bifunctional Au/Pt/Au Core/Shell Nanoraspberries for in situ SERS Monitoring of Platinum-Catalyzed Reactions. J. Am. Chem. Soc. 2011, 133 (48), 19302-19305.
14. Heck, K. N.; Janesko, B. G.; Scuseria, G. E.; Halas, N. J.; Wong, M. S. Observing Metal-Catalyzed Chemical Reactions in situ Using Surface-Enhanced Raman Spectroscopy on Pd-Au Nanoshells. J. Am. Chem. Soc. 2008, 130 (49), 16592-16600.
15. Joseph, V.; Engelbrekt, C.; Zhang, J. D.; Gernert, U.; Ulstrup, J.; Kneipp, J. Characterizing the Kinetics of Nanoparticle-Catalyzed Reactions by Surface -Enhanced Raman Scattering. Angew. Chem. Int. Ed. 2012, 51 (30), 7592-7596.
16. Huang, J. F.; Zhu, Y. H.; Lin, M.; Wang, Q. X.; Zhao, L.; Yang, Y.; Yao, K. X.; Han, Y. Site-Specific Growth of Au-Pd Alloy Horns on Au Nanorods: A Platform for Highly Sensitive Monitoring of Catalytic Reactions by Surface Enhancement Raman Spectroscopy. J. Am. Chem. Soc. 2013, 135 (23), 8552-8561.
17. Li, J. M.; Liu, J. Y.; Yang, Y.; Qin, D. Bifunctional Ag@Pd-Ag Nanocubes for Highly Sensitive Monitoring of Catalytic Reactions by Surface-Enhanced Raman Spectroscopy. J. Am. Chem. Soc. 2015, 137 (22), 7039-7042.
18. Haruta, M.; Kobayashi, T.; Sano, H.; Yamada, N. Novel Gold Catalysts for the Oxidation of Carbon-Monoxide at a Temperature Far Below 0 Degrees C. Chem. Lett. 1987, (2), 405-408.
19. Hvolbaek, B.; Janssens, T. V. W.; Clausen, B. S.; Falsig, H.; Christensen, C. H.; Norskov, J. K. Catalytic Activity of Au Nanoparticles. Nano Today 2007, 2 (4), 14-18.
20. Janssens, T. V. W.; Clausen, B. S.; Hvolbaek, B.; Falsig, H.; Christensen, C. H.; Bligaard, T.; Norskov, J. K. Insights into the Reactivity of Supported Au Nanoparticles: Combining Theory and Experiments. Top. Catal. 2007, 44 (1 -2), 15-26.
21. Abad, A.; Concepcion, P.; Corma, A.; Garcia, H. A Collaborative Effect between Gold and a Support Induces the Selective Oxidation of Alcohols. Angew. Chem. Int. Ed. 2005, 44 (26), 4066-4069.
22. Bond, G. C.; Thompson, D. T. Catalysis by Gold. Catal. Rev.-Sci. Eng. 1999, 41 (3-4), 319-388.
23. Carrettin, S.; Concepcion, P.; Corma, A.; Nieto, J. M. L.; Puntes, V. F. Nanocrystalline CeO2 Increases the Activity of an for CO Oxidation by Two Orders of Magnitude. Angew. Chem. Int. Ed. 2004, 43 (19), 2538-2540.
24. Haruta, M.; Date, M. Advances in the Catalysis of Au Nanoparticles. Appl. Catal. A-General 2001, 222 (1-2), 427-437.
25. Fujita, T.; Guan, P.; McKenna, K.; Lang, X.; Hirata, A.; Zhang, L.; Tokunaga, T.; Arai, S.; Yamamoto, Y.; Tanaka, N.; Ishikawa, Y.; Asao, N.; Yamamoto, Y.; Erlebacher, J.; Chen, M. Atomic Origins of the High Catalytic Activity of Nanoporous Gold. Nat. Mater. 2012, 11, 775.
26. Wittstock, A.; Zielasek, V.; Biener, J.; Friend, C. M.; Baumer, M. Nanoporous Gold Catalysts for Selective Gas-Phase Oxidative Coupling of Methanol at Low Temperature. Science 2010, 327 (5963), 319-322.
27. Scholl, J. A.; Koh, A. L.; Dionne, J. A. Quantum Plasmon Resonances of Individual Metallic Nanoparticles. Nature 2012, 483 (7390), 421-U68.
28. Zhang, Q. F.; Blom, D. A.; Wang, H. Nanoporosity-Enhanced Catalysis on Subwavelength Au Nanoparticles: A Plasmon-Enhanced Spectroscopic Study. Chem. Mater. 2014, 26 (17), 5131-5142.
29. Zhang, Q. F.; Large, N.; Nordlander, P.; Wang, H. Porous Au Nanoparticles with Tunable Plasmon Resonances and Intense Field Enhancements for Single-Particle SERS. J. Phys. Chem. Lett. 2014, 5 (2), 370-374.
30. Menumerov, E.; Hughes, R. A.; Neretina, S. Catalytic Reduction of 4-Nitrophenol: A Quantitative Assessment of the Role of Dissolved Oxygen in Determining the Induction Time. Nano Lett. 2016, 16 (12), 7791-7797.
31. Villarreal, E.; Li, G. F. G.; Zhang, Q. F.; Fu, X. Q.; Wang, H. Nanoscale Surface Curvature Effects on Ligand-Nanoparticle Interactions: A Plasmon-Enhanced Spectroscopic Study of Thiolated Ligand Adsorption, Desorption, and Exchange on Gold Nanoparticles. Nano Lett. 2017, 17 (7), 4443-4452.
32. Tian, N.; Zhou, Z. Y.; Sun, S. G.; Ding, Y.; Wang, Z. L. Synthesis of Tetrahexahedral Platinum Nanocrystals with High-Index Facets and High Electro-Oxidation Activity. Science 2007, 316 (5825), 732-735.
33. Zhang, Q. F.; Wang, H., Facet-Dependent Catalytic Activities of Au Nanoparticles Enclosed by High-Index Facets. ACS Catal. 2014, 4 (11), 4027-4033.
34. Zhang, Q. F.; Large, N.; Wang, H. Gold Nanoparticles with Tipped Surface Structures as Substrates for Single-Particle Surface-Enhanced Raman Spectroscopy: Concave Nanocubes, Nanotrisoctahedra, and Nanostars. ACS Appl. Mater. Interfaces 2014, 6 (19), 17255-17267.
35. Jing, H.; Zhang, Q. F.; Large, N.; Yu, C. M.; Blom, D. A.; Nordlander, P.; Wang, H. Tunable Plasmonic Nanoparticles with Catalytically Active High-Index Facets. Nano Lett. 2014, 14 (6), 3674-3682.
36. Villarreal, E.; Li, G. G.; Wang, H. Carving Growing Nanocrystals: Coupling Seed-Mediated Growth with Oxidative Etching. Nanoscale 2018, 10 (39), 18457-18462.
37. Murphy, C. J.; San, T. K.; Gole, A. M.; Orendorff, C. J.; Gao, J. X.; Gou, L.; Hunyadi, S. E.; Li, T. Anisotropic Metal Nanoparticles: Synthesis, Assembly, and Optical Applications. J. Phys. Chem. B 2005, 109 (29), 13857-13870.
38. Zhou, X. C.; Andoy, N. M.; Liu, G. K.; Choudhary, E.; Han, K. S.; Shen, H.; Chen, P. Quantitative Super-Resolution Imaging Uncovers Reactivity Patterns on Single Nanocatalysts. Nat. Nanotechnol. 2012, 7 (4), 237-241.
39. Katz-Boon, H.; Rossouw, C. J.; Weyland, M.; Funston, A. M.; Mulvaney, P.; Etheridge, J. Three-Dimensional Morphology and Crystallography of Gold Nanorods. Nano Lett. 2011, 11 (1), 273-278.
40. Goris, B.; Bals, S.; Van den Broek, W.; Carbo-Argibay, E.; Gomez-Grana, S.; Liz-Marzan, L. M.; Van Tendeloo, G. Atomic-Scale Determination of Surface Facets in Gold Nanorods. Nat. Mater. 2012, 11 (11), 930-935.
41. Katz-Boon, H.; Walsh, M.; Dwyer, C.; Mulvaney, P.; Funston, A. M.; Etheridge, J. Stability of Crystal Facets in Gold Nanorods. Nano Lett. 2015, 15 (3), 1635-1641.
42. Zhang, Q. F.; Zhou, Y. D.; Villarreal, E.; Lin, Y.; Zou, S. L.; Wang, H. Faceted Gold Nanorods: Nanocuboids, Convex Nanocuboids, and Concave Nanocuboids. Nano Lett. 2015, 15 (6), 4161-4169.
43. Zhang, Q. F.; Han, L. L.; Jing, H.; Blom, D. A.; Lin, Y.; Xing, H. L. L.; Wang, H. Facet Control of Gold Nanorods. ACS Nano 2016, 10 (2), 2960-2974.
44. Zhang, Q. F.; Jing, H.; Li, G. G.; Lin, Y.; Blom, D. A.; Wang, H. Intertwining Roles of Silver Ions, Surfactants, and Reducing Agents in Gold Nanorod Overgrowth: Pathway Switch between Silver Underpotential Deposition and Gold-Silver Codeposition. Chem. Mater. 2016, 28 (8), 2728-2741.
45. Sun, L. C.; Zhang, Q. F.; Li, G. G.; Villarreal, E.; Fu, X. Q.; Wang, H. Multifaceted Gold-Palladium Bimetallic Nanorods and Their Geometric, Compositional, and Catalytic Tunabilities. ACS Nano 2017, 11 (3), 3213-3228.
46. Li, G. G.; Lin, Y.; Wang, H. Residual Silver Remarkably Enhances Electrocatalytic Activity and Durability of Dealloyed Gold Nanosponge Particles. Nano Lett. 2016, 16 (11), 7248-7253.
47. Li, G. G.; Villarreal, E.; Zhang, Q. F.; Zheng, T. T.; Zhu, J. J.; Wang, H. Controlled Dealloying of Alloy Nanoparticles toward Optimization of Electrocatalysis on Spongy Metallic Nanoframes. ACS Appl. Mater. Interfaces 2016, 8 (36), 23920-23931.
48. Li, G. G.; Wang, H. Dealloyed Nanoporous Gold Catalysts: From Macroscopic Foams to Nanoparticulate Architectures. ChemNanoMat 2018, 4 (9), 897-908.
49. Li, G. G.; Wang, Z. X.; Blom, D. A.; Wang, H. Tweaking the Interplay among Galvanic Exchange, Oxidative Etching, and Seed-Mediated Deposition toward Architectural Control of Multimetallic Nanoelectrocatalysts. ACS Appl. Mater. Interfaces 2019, 11 (26), 23482-23494.
50. Liu, K.; Bai, Y. C.; Zhang, L.; Yang, Z. B.; Fan, Q. K.; Zheng, H. Q.; Yin, Y. D.; Gao, C. B. Porous Au-Ag Nanospheres with High-Density and Highly Accessible Hotspots for Sers Analysis. Nano Lett. 2016, 16 (6), 3675-3681.
51. Zheng, T. T.; Li, G. G.; Zhou, F.; Wu, R.; Zhu, J. J.; Wang, H. Gold-Nanosponge-Based Multistimuli-Responsive Drug Vehicles for Targeted Chemo-Photothermal Therapy. Adv. Mater. 2016, 28 (37), 8218-8226.
52. Cushing, S. K.; Li, J. T.; Meng, F. K.; Senty, T. R.; Suri, S.; Zhi, M. J.; Li, M.; Bristow, A. D.; Wu, N. Q. Photocatalytic Activity Enhanced by Plasmonic Resonant Energy Transfer from Metal to Semiconductor. J. Am. Chem. Soc. 2012, 134 (36), 15033-15041.
53. Fu, X. Q.; Li, G. G.; Villarreal, E.; Wang, H. Hot Carriers in Action: Multimodal Photocatalysis on Au@SnO2 Core-Shell Nanoparticles. Nanoscale 2019, 11 (15), 7324-7334.
54. Brongersma, M. L.; Halas, N. J.; Nordlander, P. Plasmon-Induced Hot Carrier Science and Technology. Nat. Nanotechnol. 2015, 10 (1), 25-34.
55. Zhang, G. L.; Chen, L.; Fu, X. Q.; Wang, H. Cellulose Microfiber-Supported TiO2@Ag Nanocomposites: A Dual-Functional Platform for Photocatalysis and in Situ Reaction Monitoring. Ind. Eng. Chem. Res. 2018, 57 (12), 4277-4286.
56. Zhang, Q.; Wang, H. Mechanistic Insights on Plasmon-Driven Photocatalytic Oxidative Coupling of Thiophenol Derivatives: Evidence for Steady-State Photoactivated Oxygen. J. Phys. Chem. C 2018, 122 (10), 5686-5697.